

## MATERIALS SCIENCE

# Outstanding radiation resistance of tungsten-based high-entropy alloys

O. El-Atwani<sup>1\*</sup>, N. Li<sup>2</sup>, M. Li<sup>3</sup>, A. Devaraj<sup>4</sup>, J. K. S. Baldwin<sup>2</sup>, M. M. Schneider<sup>1</sup>, D. Sobieraj<sup>5</sup>, J. S. Wróbel<sup>5</sup>, D. Nguyen-Manh<sup>6</sup>, S. A. Maloy<sup>1</sup>, E. Martinez<sup>7\*</sup>

A body-centered cubic W-based refractory high entropy alloy with outstanding radiation resistance has been developed. The alloy was grown as thin films showing a bimodal grain size distribution in the nanocrystalline and ultrafine regimes and a unique 4-nm lamella-like structure revealed by atom probe tomography (APT). Transmission electron microscopy (TEM) and x-ray diffraction show certain black spots appearing after thermal annealing at elevated temperatures. TEM and APT analysis correlated the black spots with second-phase particles rich in Cr and V. No sign of irradiation-created dislocation loops, even after 8 dpa, was observed. Furthermore, nanomechanical testing shows a large hardness of 14 GPa in the as-deposited samples, with near negligible irradiation hardening. Theoretical modeling combining ab initio and Monte Carlo techniques predicts the formation of Cr- and V-rich second-phase particles and points at equal mobilities of point defects as the origin of the exceptional radiation tolerance.

## INTRODUCTION

Key components in magnetic fusion reactors, such as the divertor or the plasma-facing materials (PFMs), are required to have stringent properties including low activation, high melting point, good thermo-mechanical properties, low sputter erosion, and low tritium retention/codeposition. They must operate at high temperature ( $\geq 1000$  K) for long durations ( $> 10^7$  s), without failure or extensive erosion while exposed to large plasma heat and an intense mixture of ionized and energetic neutral species of hydrogen isotopes (D and T), He ash (fluxes,  $> 10^{24}$  m $^{-2}$  s $^{-1}$ ), and neutrons (1). Tungsten (W) is the leading PFM candidate because of its high melting temperature, low erosion rates, and small tritium retention. These advantages are unfortunately coupled with very low fracture toughness characterized by brittle transgranular and intergranular failure regimes, which severely restrict the useful operating temperature window and also create a range of fabrication difficulties. Furthermore, blistering at moderate temperature ( $< 800$  K) by D and He (2, 3) and the formation of pits, holes, and bubbles by He at higher temperature ( $> 1600$  K) (4) have all been observed. The formation mechanisms that underpin these phenomena are not well understood but have largely been attributed to the accumulation of diffusing D and He in extended defects. In the slightly lower temperature ranging from 1250 to 1600 K, the formation of nanometer-scale bubbles is observed (5) in W exposed to the He plasma. At larger He ion fluences, close to International Thermonuclear Experimental Reactor (ITER) (6) working conditions, exposed surfaces are found to exhibit a nanostructured surface morphology (7), termed as fuzz. The increased surface area and fragility of these nanostructured surfaces raise new concerns for the use of W as a fusion reactor PFM, particularly as a source of high-Z dust that will contaminate the plasma.

Strategies such as adding different alloying elements (e.g., W-Re and W-Ti) or nanostructure-engineered W are being investigated to improve the material processing and working properties. Related to the second strategy, recent work shows that state-of-the-art nanocrystalline W samples exhibit substantial formation of He bubbles at the grain boundaries, which leads to decohesion and poor mechanical properties at operational temperatures (8–10), reducing its applicability in fusion environments. Therefore, the development of new material systems is paramount to enable fusion as a viable energy source.

In recent years, a set of alloys based on several principal elements has been developed (11–14). The configurational entropy of mixing in multicomponent alloys tends to stabilize the solid solution based on simple underlying face-centered cubic (FCC) or body-centered cubic (BCC) crystal structures. Equiatomic compositions maximize this entropic term, promoting random solutions versus intermetallic phases or phase decomposition. Some of the high-entropy alloys (HEAs) show superior mechanical response to traditional materials, which generally links to dislocation properties. These materials can display high hardness values, high yield strengths, large ductility, excellent fatigue resistance, and good fracture toughness. W-based refractory HEAs have been recently developed in the context of high-temperature applications, showing high melting temperature (above 2873 K) and superior mechanical properties at high temperatures compared to Ni-based superalloys and nanocrystalline W (15) samples (16, 17).

HEAs have been also studied under irradiation, mostly for FCC crystalline structures. Zhang *et al.* (18) showed how chemical complexity can lead to a variation in the thermodynamic and kinetic properties of defects that might modify the microstructure evolution under irradiation. They linked the amount of irradiation-created defects and defect properties to electron and phonon mean free paths and dissipation mechanisms that could be tuned in these alloys by varying their composition. Granberg *et al.* (13) combined experiments and modeling to identify the sluggish mobility of dislocation loops as the main mechanism leading to radiation tolerance in Ni-based FCC HEAs. Kumar *et al.* (19) showed how Ni-based FCC HEAs lead to less radiation-induced segregation and fewer voids, although hardness was observed to increase after irradiation. Other studies show results in the same direction, with HEAs improving radiation tolerance in both FCC and BCC structures (20–22). Very recently, W-based quinary HEAs

<sup>1</sup>Materials Science and Technology Division, Los Alamos National Laboratory, Los Alamos, NM, USA. <sup>2</sup>Center for Integrated Nanotechnologies, MPA-CINT, Los Alamos National Laboratory, Los Alamos, NM 87545, USA. <sup>3</sup>Division of Nuclear Engineering, Argonne National Laboratory, Argonne, IL, USA. <sup>4</sup>Physical and Computational Sciences Directorate, Pacific Northwest National Laboratory, Richland, WA, USA. <sup>5</sup>Faculty of Materials Science and Engineering, Warsaw University of Technology, Ulica Wołoska 141, 02-507 Warsaw, Poland. <sup>6</sup>Department of Materials Science and Scientific Computing, CCFE, United Kingdom Atomic Energy Authority, Abingdon, Oxfordshire OX14 3DB, UK. <sup>7</sup>Theoretical Division, T-1, Los Alamos National Laboratory, Los Alamos, NM, USA.

\*Corresponding author. Email: oelatwan25@gmail.com (O.E.); enriquem@lanl.gov (E.M.)

with diverse composition have been synthesized as potential materials for fusion applications. The authors observed the formation of Ti carbides and laves phases at large W concentrations. The authors studied the mechanical response, showing that these materials could lead to twofold improvement in the hardness and strength due to solid solution strengthening and dispersion strengthening (23). However, refractory HEAs have never been tested under irradiation for potential uses as PFMs or structural materials in nuclear fusion environments. In this work, we have developed a quaternary nanocrystalline W-Ta-V-Cr alloy that we have characterized under thermal conditions and after irradiation. Note that the possible combination of elements to synthesize an HEA is exceedingly large. To narrow the possible candidate systems, we have to bear in mind that high-Z materials are generally desirable to minimize sputtering. In addition, low-activation elements must be considered to reduce radiotoxicity, which excludes the use of Ni, Cu, Al, Mo, Co, or Nb. Furthermore, Fe and Mn usually form intermetallics, which might induce a more complex behavior. Thus, W, Ta, V, and Cr were chosen as testing ingredients for the target system. We show how this alloy can be synthesized using a magnetron sputtering deposition system. Both energy dispersive spectroscopy (EDS) analysis, which measures chemical composition, and atom probe tomography (APT) indicate W and Ta enrichment in the deposited films. The EDS mapping on both surface and cross-sectional areas and x-ray diffraction (XRD) results show a single-phase BCC after deposition. The samples were irradiated with 1-MeV Kr<sup>+2</sup> in situ at the Intermediate Voltage Electron Microscope (IVEM)-Tandem Facility at Argonne National Laboratory up to 8 displacements per atom (dpa) with no sign of irradiation-created defects. Moreover, nanoindentation tests were also performed, showing hardness of the film on the order of ~15 GPa.

## RESULTS

### HEA morphology and thermal stability

A detailed characterization of the morphology and phase details of the as-deposited HEA films results in a bimodal grain size distribution with ~70% of the grains with size in the nanocrystalline regime ( $\leq 100$  nm) and some regions of ultrafine grain sizes (100 to 500 nm) with an underlying single-phase BCC, with a lattice constant of ~3.2 Å (see the Supplementary Materials). Before irradiation, we performed EDS (Fig. 1) and APT (Fig. 2) to investigate the composition of this alloy. EDS line scan (Fig. 1A) was performed to determine the composition in the alloy (Fig. 1B), while EDS mapping (Fig. 1C) shows uniform elemental composition. APT confirmed the EDS results, showing a film composition of 38% ( $\pm 0.09$ ) W, 36% ( $\pm 0.09$ ) Ta, 15% ( $\pm 0.05$ ) Cr, and 11% ( $\pm 0.05$ ) V. The three-dimensional (3D) distribution of elements, determined via APT, in the film before irradiation is shown in Fig. 2 (A to D), while the 2D compositional maps using a slice of APT data with a size of 25 nm by 1 nm by 20 nm are shown in Fig. 2 (E to J) where the color scale bars below each figure highlight the high and low concentration values for each element. The morphology is composed of very distinct compositional striations (layering) within the grains of ~4-nm thickness, which was not observed in EDS. We also found evidence for element segregations to the grain boundaries, as shown in the three distinct grain boundaries captured by APT (Fig. 2, I to L).

We studied the thermal stability of these films in situ using transmission electron microscopy (TEM) with temperatures up to 1073 K (see fig. S2). Changes in grain sizes were not observed. Above 1023 K,

some grains exhibited black spots (slight segregation of certain elements). We also checked the nanoscale distribution of elements with APT analysis for an annealed sample at 1050 K (see fig. S3). Clear compositional layering is visible in both the ion maps and the 2D compositional maps. The segregation of elements to grain boundaries was also observed to be similar to as-deposited films. No evidence for disappearance of compositional striations or clustering of elements was observed in the APT results, indicating that compositional clustering was not homogeneously distributed in the sample after heating. Not all grains demonstrated compositional clustering, indicating grain variations regarding elemental segregation.

### Irradiation

We then irradiated the HEA films in situ at the IVEM-Tandem Facility with 1-MeV Kr<sup>+2</sup> and 1073 K, with a dpa rate of 0.0006 dpa s<sup>-1</sup> to 1.6 dpa (fig. S4). During irradiation, no dislocation loops were observed. However, further and enhanced precipitation (black spot formation) was recognized. A higher dpa irradiation was then performed on a different film at the same temperature (1073 K) with a dpa rate of 0.0016 dpa s<sup>-1</sup> to 8 dpa. The morphology during irradiation is shown in Fig. 3 (see also movies S1 and S2 for low and high doses, respectively). Precipitation was shown to occur during irradiation, where its intensity increased with dose. Notably, dislocation loops were not observed even at 8 dpa.

We also performed irradiations at room temperature and a dose rate of 0.0006 dpa s<sup>-1</sup> to 1.6 dpa (see fig. S4 and movie S3 for low dose). No dark spot formation was observed, and no dislocation loops were shown to form.

Furthermore, we investigated the mechanical properties of this material on thicker films (~3 μm) before irradiation, after annealing, and after ex situ irradiation with 3-MeV Cu<sup>+</sup> to a peak dose of ~17 dpa (with a dose rate of 0.02 dpa s<sup>-1</sup>) via nanoscale dynamic mechanical analysis (nanoDMA). Representative load versus displacement curves show a shift to the left in the loading curves, indicating an increase in hardness, which is confirmed by the hardness versus displacement curves. The annealing process results in a hardness increase, which is slightly enhanced by irradiation (see fig. S6).

## DISCUSSION

### Precipitation versus loop formation

As it has been already mentioned above, the nucleation and growth of black spots was observed in the sample during annealing at elevated temperatures (1023 K). Their intensity slightly increased with irradiation, and there was no apparent loop formation. Precipitates can be distinguished from dislocation loops using a TEM procedure, which was detailed by Jenkins (24). The procedure consists of analyzing the change in the  $\mathbf{l}$  vector (a vector that runs from the center of the black spot to the white area) and the change in diffraction condition ( $\mathbf{g}$  vector). For precipitates with symmetrical strain field, the  $\mathbf{l}$  vector would follow the  $\mathbf{g}$  vector when tilting the specimen to different  $\mathbf{g}$  beams (vectors). However, dislocation loop  $\mathbf{l}$  vectors are tied to the Burgers vector and would not rotate from one  $\mathbf{g}$  vector to another. However, this procedure breaks down when precipitates have asymmetric strain fields or when dislocation loops are not of edge character (24). Moreover, in nanocrystalline samples with small grains, performing this procedure is extremely challenging. We have used two different techniques, TEM and APT analysis, to confirm that the black spots observed in our irradiated samples are precipitates.

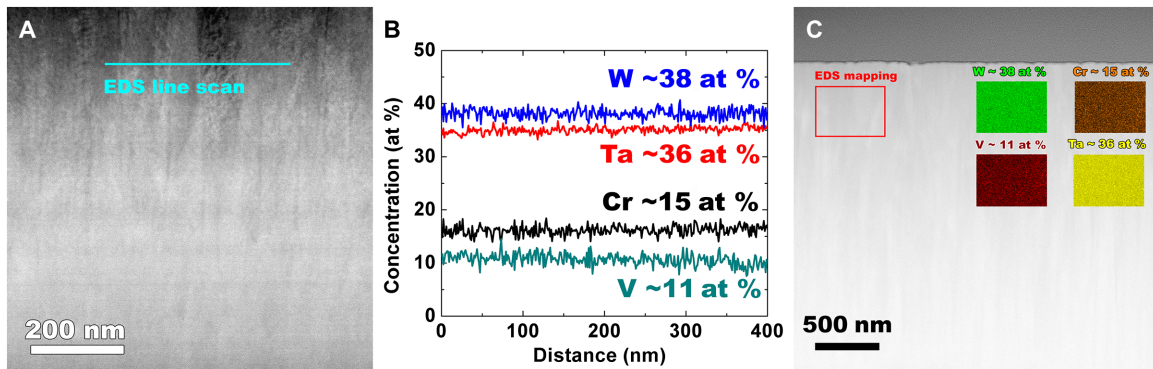


**Fig. 1. Alloy composition.** (A) Cross-sectional transmission electron microscopy (TEM) image of the HEA film showing a region where EDS line scan is performed. (B) EDS line scan concentration profiles of the elements in the HEA film. (C) Cross-sectional scanning electron microscopy micrograph with EDS maps of the elemental composition on the HEA film.

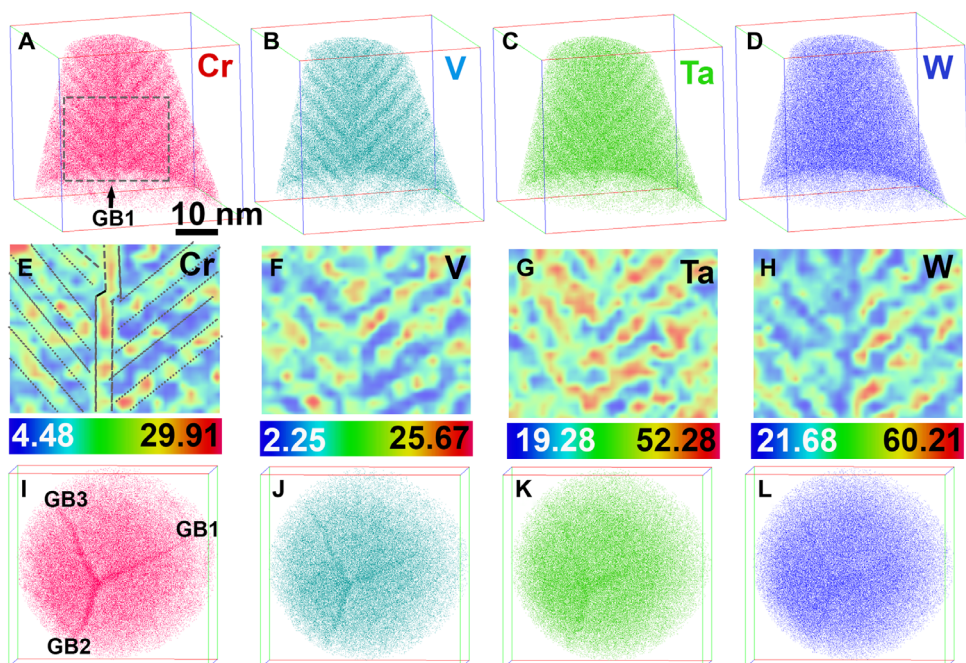


**Fig. 2. APT analysis of the as-received HEA.** (A) to (D) 3D distribution of Cr, V, Ta, and W. (E) to (H) 2D compositional maps with the color bars denote the concentration range for each element. (I) to (L) top-down view of three different GBs.

Downloaded from https://www.science.org on December 22, 2022

### TEM investigation of the black spots

The HEA-irradiated films are of BCC type. Although precipitation occurred, electron diffraction (Fig. 3I) showed only BCC-related rings. For a BCC material, the Burgers vector of irradiation-created dislocation loops can be of  $\langle 111 \rangle$  or  $\langle 100 \rangle$  type (25, 26). Therefore, there are seven possibilities of Burgers vector variants (four for  $\langle 111 \rangle$  type and three for  $\langle 100 \rangle$  type). In W-related materials, the Burgers vector of  $\langle 111 \rangle$  type has been observed at 1073 K (25, 27, 28). Under any diffraction conditions, using the  $\mathbf{g} \cdot \mathbf{b}$  invisibility criteria, at least 50% of the  $\langle 111 \rangle$  loops should be observed in the TEM image. However, in our samples, several grains showed no black spots (e.g., as shown in Fig. 3).

This observation can be confirmed via two-beam imaging with TEM. Figure 4A shows an on-zone image of a 200-nm grain with black spots. The sample was then tilted to get a two-beam image with the  $\langle 211 \rangle \mathbf{g}$  vector. Using a  $\langle 211 \rangle \mathbf{g}$  vector, both  $\langle 111 \rangle$  and  $\langle 100 \rangle$

dislocation loop should be visible in the image. However, no loops were observed (Fig. 4B).

### APT analysis

APT was performed on a sample irradiated at 1050 K to  $\sim 8$  dpa using 3-MeV  $\text{Cu}^+$ . After irradiation, we observed no compositional layering of any element (Fig. 5, A to H). Although elemental segregation at grain boundaries is still observed, the precipitation of Cr-rich phases in the grain matrices occurred, as shown in the top-down view of an APT reconstruction with a 25 atomic % (at %) Cr isocomposition surface (Fig. 5, M and N). We have also analyzed the compositional partitioning between the precipitate and the grain matrix (Fig. 5O), showing the enrichment of Cr and V and the depletion of W and Ta inside the black spots. These precipitates are of  $\sim 3$  to 5 nm in size and show a density of  $\sim 0.03 \text{ nm}^{-2}$ , both of which are consistent with the



**Fig. 3.** Bright-field TEM micrographs as a function of dpa of in situ  $1\text{-MeV } \text{Kr}^{+2}$ -irradiated HEA at 1073 K using a dpa rate of  $0.0016 \text{ dpa s}^{-1}$ . (A) Pre-irradiation, (B) 0.2 dpa, (C) 0.6 dpa, (D) 1.0 dpa, (E) 1.6 dpa, (F) 3.2 dpa, (G) 4.8 dpa, (H) 6.4 dpa, and (I) 8 dpa. Images show enhanced precipitation (black spots formation) in some grains. All images have the same scale bar.

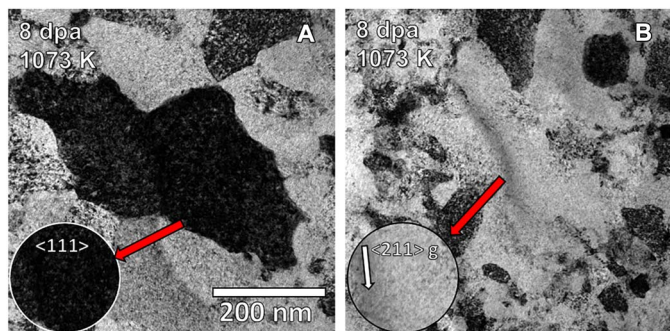


**Fig. 4.** Post-irradiation bright-field TEM micrographs of 8-dpa  $1\text{-MeV } \text{Kr}^{+2}$ -irradiated HEA at 1073 K using a dpa rate of  $0.0016 \text{ dpa s}^{-1}$ . Post-irradiation bright-field TEM micrographs of 8 dpa  $1\text{-MeV } \text{Kr}^{+2}$ -irradiated HEA at 1073 K using a dpa rate of  $0.0016 \text{ dpa s}^{-1}$ . (A) Using  $<111>$  on-zone imaging showing small black spots (precipitates). (B) Two-beam image with  $<211> \mathbf{g}$  vector showing no black spots. Insets: Magnified images. Both images have the same scale bar.

in situ-irradiated 8-dpa sample (similar size and density). Therefore, we can conclude that the black spots observed in the irradiated HEA samples at high temperature are Cr- and V-rich precipitates and not irradiation-created dislocation loops.

#### Origin of Cr- and V-rich precipitates in the HEAs

To understand the origin of the Cr- and V-rich precipitates observed in annealed and irradiated HEA samples, we have systematically carried out first-principles calculations of phase stability and chemical short-range order (SRO) of the multicomponent 38 at % W/36 at % Ta/15 at % Cr/11 at % V alloy as a function of temperature. The cluster expansion (CE) methodology [see Methods and refs. (29–32)] has been used to build up an ab initio-based Hamiltonian with many-body effective cluster interactions (ECIs), from which the configurational entropy and therefore the free energy of multicomponent system can be obtained from thermodynamic integration techniques (29) in combination with canonical Monte Carlo (CMC) simulations.

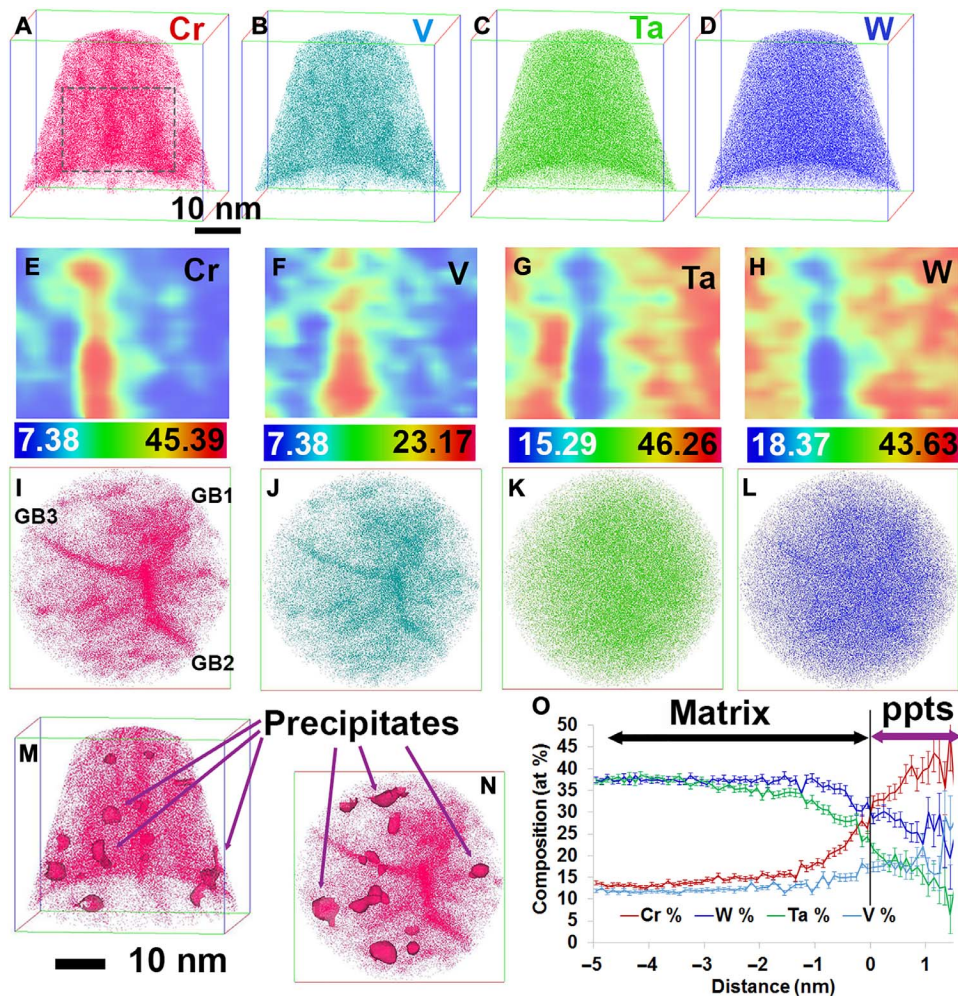


**Fig. 5.** APT analysis of the HEA irradiated to 8 dpa with 3-MeV Cu<sup>+</sup> at 1050 K. (A) to (D) 3D distribution of Cr, V, Ta, and W. (E) to (H) 2D compositional maps of Cr, V, Ta, and W using a slice of 25 nm by 1 nm by 20 nm. (I) to (L) Top-down view showing the location of three different GBs and the corresponding elemental segregation. Reconstruction side-view (M) and top-view (N) with 25 at % Cr isocomposition surface showing Cr-V-rich precipitates inside grains. (O) Compositional partitioning between the precipitate and the matrix. ppts, precipitates.

The enthalpies of mixing were calculated using the density functional theory (DFT) and CE methods for nearly 270 structures within the BCC underlying crystalline lattice. Values for all binary structures in the database were analyzed to determine the nature of the atomic interactions in all possible binary configurations (fig. S7). The positive and negative enthalpies of mixing values indicate a tendency for segregation or ordering, respectively.

In agreement with previous DFT/CE studies for W-Ta and W-V systems (33), it is found that the enthalpies of mixing for these two binaries are negative for the whole compositional range, a trend followed also by the Cr-V binary. This behavior is characteristic of alloys between the BCC transition metals of groups V and VI of the periodic table of elements from first principles-based electronic structure calculations (34). For the Cr-Ta system, besides the small negative enthalpies of mixing, again due to mixing between elements of the two groups, there are also positive values. It is explained by the fact that, along with the chemical bonding, the difference of atomic size between the 3d (Cr: R<sub>a</sub> = 0.130 nm) and 5d (Ta: R<sub>a</sub> = 0.143 nm) transition metals plays also an important role in the enthalpy of mixing. In contrast, it is found that the enthalpies of mixing between the transition

metals of the same groups V (Ta-V binary) and VI (Cr-W binary) are positive within the whole concentration range. The analysis of the chemical ordering with the Warren-Cowley SRO parameters (35) results in a strong segregation tendency of Cr and V, as can be seen in Fig. 6A (see also the Supplementary Materials).

We observe the precipitation of Cr-V-rich particles at both room temperature and 1000 K (see Fig. 6B). To determine the local concentration of each element across the Cr-V-rich phase, we have subdivided the system in 2D cells of 12 Å by 12 Å and calculated the average concentration in every cell. The resulting concentration profile is shown in Fig. 6C. The composition inside the Cr-V-rich phase is found to be 62 at % Cr, 30 at % V, 5 at % W, and 3 at % Ta. Comparing with the compositional partitioning between the precipitates and matrix found experimentally (see Fig. 5O), we observed that a very similar trend of strong Cr segregation along with V is well reproduced from our atomistic simulations. The slight difference in composition might be a kinetic effect, i.e., a result of the fact that irradiation modifies the steady-state microstructure of the system.

The results of this modeling analysis, showing the phase separation of Cr-V-rich precipitates, are fully consistent with the compositional

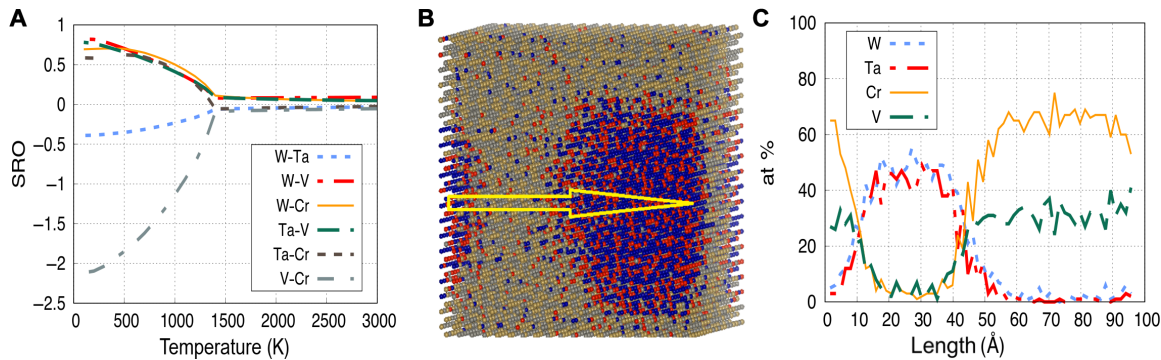


**Fig. 6. Theoretical predictions of the atomic configurations.** (A) Average SRO parameters in the  $\text{W}_{38}\text{Ta}_{36}\text{Cr}_{15}\text{V}_{11}$  alloy as a function of temperature. (B) Atomic configuration in the  $\text{W}_{38}\text{Ta}_{36}\text{Cr}_{15}\text{V}_{11}$  alloy at  $T = 1000$  K after CMC simulations. (C) Average concentration profile of each element along the  $[001]$  direction across the Cr-V cluster.

layering features observed in the APT results for the as-deposited samples (Fig. 2, E to H) and for the thermal stability investigations (fig. S3, E to H). The fact that precipitation is also observed under irradiation is also consistent with the modeling results that highlight a strong thermodynamic force for the system to phase separate.

#### Irradiation tolerance of the HEA

To correlate the experimental observations with the properties of irradiation-created defects, we rely on a reaction rate model in which the reaction probability per unit time of two defects moving in 3D is given by (36)

$$R = 4\pi r_c \frac{D_i + D_j}{\Omega_a}$$

where  $r_c$  is a given capture radius,  $D_i$  and  $D_j$  are the diffusion coefficients of two defects (different or alike), and  $\Omega_a$  is the atomic volume. For two defects of the same type, this gives the probability per unit time of forming a cluster, and if the defects are different, this is the recombination probability. The ratio between the recombination probability and the clustering probability is maximum when the mobilities of the different defects are equal. The fact that no clustering is experimentally observed indicates that, in the HEA described in this work, this is a plausible case, i.e., the mobilities of vacancies and self-interstitials are similar as oppose to what happens in pure W, with a great disparity in defect mobilities (37–39). Maximizing recombination will lead to a reduction in defect concentration and therefore a reduction in the kinetics of precipitation and growth of second-phase particles. Equal mobilities must be a consequence of the rough energy landscape induced by the local lattice distortion and the disparity in chemistry.

The presence of a high density of grain boundaries will also lead to a reduction of the defect concentrations, as grain boundaries are usually preferential recombination/annihilation sites for defects. However, even nanocrystalline W with grain sizes on the order of the ones studied here shows the formation of large irradiation-created dislocation loops that diffuse to grain boundaries. The fact that defect clusters are not observed in the HEA leads again to the fact that the concentration of defects inside the grains is minimized by the fact that their mobilities are similar. It is also worth mentioning that the effect of precipitates on the recombination probability does not seem to be large since, at low temperature, although there is no appreciable precipitate density, there are still no dislocation loops observed.

#### CONCLUSIONS

The present work shows the development of a new class of a refractory HEA based on four elements: 38% W, 36% Ta, 15% Cr, and 11% V in atomic percentages measured by both EDS and APT. Samples were grown using a magnetron sputtering deposition system from pure metal targets and characterized before and after irradiation. Microstructures present a single-phase BCC crystalline structure. The films show a bimodal grain size distribution with ~70% of the grains with sizes in the nanocrystalline regime ( $\leq 100$  nm) and some regions of ultrafine grain sizes (100 to 500 nm). Concurrent TEM and APT analyses demonstrate the existence of a second phase rich in Cr and V, first forming lamella-like regions to transform to quasi-spherical precipitates after irradiation. Irradiations were carried out both in situ and ex situ at room temperature and 1073 K up to 8 dpa. A thorough analysis of the microstructure shows no sign of radiation-induced dislocation loops, confirming that the observed black spots are indeed second-phase particles. APT results show the segregation of Cr and V to grain boundaries and triple junctions. The mechanical properties of the system have been also investigated through nanoindentation. A hardness of about 14 GPa was obtained for the as-deposited sample, increasing slightly after thermal annealing and after irradiation, with small reported irradiation hardening. Accompanying modeling has also been performed. An energetic model for the four-component system has been developed on the basis of a CE formalism. Monte Carlo simulations were subsequently carried out with the underlying energetics to find out the equilibrium properties of the system. Our DFT-based CMC simulations show phase decomposition in marked agreement with the experimental results. A rate theory model ties the outstanding irradiation resistance properties to the defect mobilities and their recombination probability, which are optimal in these systems. The fact that these alloys are suitable for bulk production coupled with the exceptional radiation resistance makes them ideal structural materials for applications requiring extreme irradiation conditions.

#### METHODS

##### Experimental methodology

##### Preparation of W-Ta-Cr-V alloy

The films were prepared via magnetron sputtering deposition system from pure metal targets of 99.99% purity using deposition powers of 192, 312, 277, and 300 W for Cr, V, Ta, and W, respectively, and a bias radio frequency power of 20 W. The deposition was performed at

room temperature and 3 mtorr pressure with no bias voltage. Films (approximately 100 nm) were prepared on NaCl salt using the above parameters with 60-s deposition. For the TEM work, TEM samples of the 100-nm films deposited on NaCl were prepared by floating the film on a standard molybdenum TEM grid using 1:1 ethanol/water solution. For XRD and nanoindentation work, thicker films were deposited on silicon using the same parameters with 3000-s deposition time. We did not find any substantial porosity in the material through TEM analysis.

#### *In situ TEM/irradiation*

In situ Kr<sup>+2</sup> ion irradiation with 1 MeV was performed using the IVEM attached to a tandem accelerator at Argonne National Laboratory. The experiments were performed at room temperature and 1073 K. The electron beam energy was 300 keV. The average dose rate was 0.0006 and 0.0016 dpa s<sup>-1</sup> for the samples irradiated to a final dose of 1.6 and 8 dpa, respectively. A charge-coupled device camera with a resolution of 4000 by 4000 was used to capture the video and still images at different doses. The dpa values were calculated (see fig. S10) using the Kinchin-Pease model in the stopping and range of ions in matter Monte Carlo computer code (version 2013) (40), and 40 eV (41) was taken as the displacement threshold energy for all elements. The atomic percentages of the elements were 38% W, 36% Ta, 15% Cr, and 11% V. Before the in situ experiment, the samples were annealed in situ inside the TEM with a Gatan heating holder at 1123 K.

#### *Ex situ irradiation*

Ex situ irradiation on the ~3-μm-thick HEA films was performed in the Ion Beam Materials Laboratory at Los Alamos National Laboratory (LANL) using the tandem accelerator with 3-MeV Cu<sup>+</sup> ions at nominal incidence. The irradiations were performed at 773 and 1050 K using a dose rate of 0.0167 dpa s<sup>-1</sup>. The dpa of the first 100 nm (to have similar dpa to the 100-nm TEM samples in the in situ TEM/irradiation work) was ~7.5 dpa, which corresponds to a peak dose of ~17 dpa at 650 nm (see fig. S10).

#### *Characterization*

The characterization of the films before irradiation was performed using XRD and TEM to investigate the existing phases in the films and the overall microstructure. In addition to the in situ images taken at the IVEM-Tandem Facility, post-characterization was also performed using FEI Tecnai F30 TEM operating at 300 keV and FEI Titan 80–300 TEM operating at 300 keV. APT was performed on three HEA films: (i) pristine, (ii) annealed to 1050 K, and (iii) irradiated with 3-MeV Cu<sup>+</sup> to ~8 dpa. Needle specimens for APT analysis were prepared using an FEI Quanta 3D DualBeam focused ion beam system through a lift-out and annular milling process (42). APT analysis was conducted using a CAMECA LEAP 4000XHR system in laser-assisted mode using a 40-pJ laser pulse energy, with a 355-nm ultraviolet laser at 125-kHz pulse frequency while maintaining the specimen temperature at 40 K and detection rate at 0.005 atoms per pulse. The APT data were reconstructed using Integrated Visualization and Analysis Software (IVAS) 3.8 APT data analysis software.

#### *Nanoindentation*

Nanoindentation was performed on a Hysitron Tribo950 using the low-force transducer, nanoDMA, and a diamond Berkovich (three-sided pyramidal) tip. The nanoDMA technique allows for the continuous measurement of modulus and hardness with depth by oscillating the tip at a prescribed frequency and displacement or load amplitude, which is equivalent to many small unloads. A nanoDMA frequency of 100 Hz and displacement amplitude of 2 nm were used. Tests were run to a final load of 10 mN and for a total test time of 35 s using a constant strain

rate load function. Indents were made on the 3-MeV Cu<sup>+</sup>-irradiated samples (thick films). Samples were fixed to magnetic discs with super glue and magnetically held on the nanoindenter stage. The hardness was determined using the Oliver-Pharr method (43) with an area function calibrated on fused silica. The average hardness was taken at a displacement range of 100 to 150 nm. We estimate that this corresponds to interacting with a material down to 450 nm (three times the displacement) based on the work by Hardie *et al.* (44)

#### **Modeling methodology**

In the CE formalism, the enthalpy of mixing of a *K* component alloy system is defined in the form of Ising-like Hamiltonian as

$$\Delta H_{CE}(\vec{\sigma}) = \sum_{\omega} m_{\omega} J_{\omega} (\langle \Gamma_{\omega}(\vec{\sigma}) \rangle_{\omega})$$

where an atomic configuration is specified by a vector of the configurational variables  $\vec{\sigma}$ . The summation was performed over all distinct clusters  $\omega$  under group symmetry operations of the underlying lattice. The parameters  $m_{\omega}$  are multiplicities indicating the number of clusters equivalent to  $\omega$  by symmetry,  $J_{\omega}$  are the concentration-independent ECI parameters, and  $\langle \Gamma_{\omega}(\vec{\sigma}) \rangle$  denotes the cluster functions defined as products of point functions of occupation variables on a specific cluster  $\omega$  averaged over all the clusters  $\omega'$  that are equivalent by symmetry to cluster  $\omega$ . In a *K* component system, a cluster function is defined as a product of orthogonal point functions  $\gamma_{j_1, K}(\sigma_1)$ ,

$$\Gamma_{\omega, n}^{(s)}(\vec{\sigma}) = \gamma_{j_1, K}(\sigma_1) \gamma_{j_2, K}(\sigma_2) \dots \gamma_{j_{|\omega|}, K}(\sigma_{|\omega|})$$

where the sequence  $(s) = (j_1 j_2 \dots j_{|\omega|})$  is the decoration (29) of the cluster by point functions. The number of possible decorations of clusters by nonzero point functions is a permutation with repetitions,  $(K - 1)^{|\omega|}$ . The occupation variables and point functions are defined in such a way that it is possible to use the same formulae for *K* component systems

$$\gamma_{j, K}(\sigma_i) = \begin{cases} 1 & \text{if } j = 0 \\ -\cos\left(2\pi\left[\frac{j}{2}\right]\frac{\sigma_i}{K}\right) & \text{if } j > 0 \text{ and odd} \\ -\sin\left(2\pi\left[\frac{j}{2}\right]\frac{\sigma_i}{K}\right) & \text{if } j > 0 \text{ and even} \end{cases}$$

where  $\sigma_i = 0, 1, 2, \dots, (K - 1)$ ,  $j$  is the index of point functions [ $j = 0, 1, 2, \dots, (K - 1)$ ], and where  $\left[\frac{j}{2}\right]$  denotes an operation where we take the integer plus one value of a noninteger number. To compute ECIs from first principles, the structure inversion method (SIM) was used. In SIM, energies were computed using DFT for a series of structures, the cluster functions were calculated for these structures, and a set of linear equations was constructed, from which the unknown ECIs can be obtained through least-squares fitting. It is also important to note that, although ECIs are assigned to ideal lattice sites, they are fit to the energies of fully relaxed structures. The displacements off the ideal sites caused by size and chemical composition variations are thus included implicitly via relaxed total energy calculations. The accuracy of CE models was usually estimated by the cross-validation (CV) value that indicates the predictive power of the CE. It is defined as the square root mean of differences between those calculated from

first principles and the energies predicted from the CE for structures that were not used in the fitting

$$CV = \sqrt{\frac{1}{n} \sum_{i=1}^n (E_i - \hat{E}_{(i)})^2}$$

where  $E_i$  is the energy of structure  $i$  calculated using DFT, and  $\hat{E}_{(i)}$  is the energy of that structure predicted using CE.

## SUPPLEMENTARY MATERIALS

Supplementary material for this article is available at <http://advances.sciencemag.org/cgi/content/full/5/3/eaav2002/DC1>

Section S1. HEA morphology and thermal stability

Section S2. Thermal stability

Section S3. Irradiation

Section S4. Mechanical properties

Section S5. Enthalpies of mixing

Section S6. Chemical ordering

Section S7. Dose values

Fig. S1. Alloy structure.

Fig. S2. Bright-field TEM micrographs W-Ta-Cr-V HEA alloy as a function of time during the thermal stability experiment performed in situ with TEM, showing no change in the grain sizes of the nanocrystalline or the ultrafine grains but slight black spots in some grains (precipitation).

Fig. S3. APT analysis of the HEA after annealing at 1050 K.

Fig. S4. Bright-field TEM micrographs as a function of dpa of in situ 1-MeV Kr<sup>+2</sup>-irradiated HEA at 1073 K using a dpa rate of 0.0006 dpa s<sup>-1</sup>.

Fig. S5. Bright-field TEM micrographs as a function of dpa of in situ 1-MeV Kr<sup>+2</sup>-irradiated HEA at room temperature using a dpa rate of 0.0006 dpa s<sup>-1</sup>.

Fig. S6. Mechanical response of the HEA.

Fig. S7. Enthalpies of mixing of all binary alloys in the quaternary W-Ta-Cr-V system obtained from DFT and CE calculations.

Fig. S8. Average SRO parameters in the W<sub>38</sub>Ta<sub>36</sub>Cr<sub>15</sub>V<sub>11</sub> alloy as a function of temperature.

Fig. S9. Atomic configurations for a W<sub>38</sub>Ta<sub>36</sub>Cr<sub>15</sub>V<sub>11</sub> alloy obtained from MC simulations.

Fig. S10. Ion and displacement damage distribution of 1-MeV Kr<sup>+2</sup> and 3-MeV Cu<sup>+</sup> in the HEA.

Movie S1. Irradiation of the HEA films at low dose and 1073 K.

Movie S2. Irradiation of the HEA films at high dose and 1073 K.

Movie S3. Irradiation of the HEA films at room temperature.

## REFERENCES AND NOTES

- M. J. Baldwin, R. P. Doerner, Helium induced nanoscopic morphology on tungsten under fusion relevant plasma conditions. *Nucl. Fusion*. **48**, 035001 (2008).
- W. M. Shu, G.-N. Luo, T. Yamanishi, Mechanisms of retention and blistering in near-surface region of tungsten exposed to high flux deuterium plasmas of tens of eV. *J. Nucl. Mater.* **367–370**, 1463–1467 (2007).
- S. Nagata, B. Tsuchiya, T. Sugawara, N. Ohtsu, T. Shikama, Helium and hydrogen trapping in W and Mo single-crystals irradiated by He ions. *J. Nucl. Mater.* **307**, 1513–1516 (2002).
- D. Nishijima, M. Y. Ye, N. Ohno, S. Takamura, Incident ion energy dependence of bubble formation on tungsten surface with low energy and high flux helium plasma irradiation. *J. Nucl. Mater.* **313–316**, 97–101 (2003).
- D. Nishijima, M. Y. Ye, N. Ohno, S. Takamura, Formation mechanism of bubbles and holes on tungsten surface with low-energy and high-flux helium plasma irradiation in NAGDIS-II. *J. Nucl. Mater.* **329–333**, 1029–1033 (2004).
- ITER—The way to new energy. *ITER*; [www.iter.org](http://www.iter.org).
- S. Takamura, N. Ohno, D. Nishijima, S. Kajita, Formation of nanostructured tungsten with arborecent shape due to helium plasma irradiation. *Plasma Fusion Res.* **1**, 051 (2006).
- O. El-Atwani, S. Gonderman, S. Suslov, M. Efe, G. De Temmerman, T. Morgan, K. Bystrøv, K. Hattar, J. P. Allain, Early stage damage of ultrafine-grained tungsten materials exposed to low energy helium ion irradiation. *Fusion Eng. Des.* **93**, 9–14 (2015).
- O. El-Atwani, K. Hattar, J. A. Hinks, G. Greaves, S. S. Harilal, A. Hassanein, Helium bubble formation in ultrafine and nanocrystalline tungsten under different extreme conditions. *J. Nucl. Mater.* **458**, 216–223 (2015).
- O. El-Atwani, A. Suslova, T. J. Novakowski, K. Hattar, M. Efe, S. S. Harilal, A. Hassanein, In-situ TEM/heavy ion irradiation on ultrafine-and nanocrystalline-grained tungsten: Effect of 3 MeV Si, Cu and W ions. *Mater. Charact.* **99**, 68–76 (2015).
- M. C. Gao, J.-W. Yeh, P. K. Liaw, Y. Zhang, *High-Entropy Alloys* (Springer International Publishing, 2016); <http://link.springer.com/10.1007/978-3-319-27013-5>.
- D. B. Miracle, High-entropy alloys: A current evaluation of founding ideas and core effects and exploring “nonlinear alloys”. *JOM* **69**, 2130–2136 (2017).
- F. Granberg, K. Nordlund, M. W. Ullah, K. Jin, C. Lu, H. Bei, L. M. Wang, F. Djurabekova, W. J. Weber, Y. Zhang, Mechanism of radiation damage reduction in equiatomic multicomponent single phase alloys. *Phys. Rev. Lett.* **116**, 135504 (2016).
- D. B. Miracle, O. N. Senkov, A critical review of high entropy alloys and related concepts. *Acta Mater.* **122**, 448–511 (2017).
- O. El-Atwani, J. A. Hinks, G. Greaves, J. P. Allain, S. A. Maloy, Grain size threshold for enhanced irradiation resistance in nanocrystalline and ultrafine tungsten. *Mater. Res. Lett.* **5**, 343–349 (2017).
- O. N. Senkov, G. B. Wilks, J. M. Scott, D. B. Miracle, Mechanical properties of Nb<sub>25</sub>Mo<sub>25</sub>Ta<sub>25</sub>W<sub>25</sub> and V<sub>20</sub>Nb<sub>20</sub>Mo<sub>20</sub>Ta<sub>20</sub>W<sub>20</sub> refractory high entropy alloys. *Intermetallics* **19**, 698–706 (2011).
- Y. Zou, H. Ma, R. Spolenak, Ultrastrong ductile and stable high-entropy alloys at small scales. *Nat. Commun.* **6**, 7748 (2015).
- Y. Zhang, G. Malcolm Stocks, K. Jin, C. Lu, H. Bei, B. C. Sales, L. Wang, L. K. Béland, R. E. Stoller, G. D. Samolyuk, M. Caro, A. Caro, W. J. Weber, Influence of chemical disorder on energy dissipation and defect evolution in concentrated solid solution alloys. *Nat. Commun.* **6**, 8736 (2015).
- N. A. P. K. Kumar, C. Li, K. J. Leonard, H. Bei, S. J. Zinkle, Microstructural stability and mechanical behavior of FeNiMnCr high entropy alloy under ion irradiation. *Acta Mater.* **113**, 230–244 (2016).
- C. Lu, L. Niu, N. Chen, K. Jin, T. Yang, P. Xiu, Y. Zhang, F. Gao, H. Bei, S. Shi, M.-R. He, I. M. Robertson, W. J. Weber, L. Wang, Enhancing radiation tolerance by controlling defect mobility and migration pathways in multicomponent single-phase alloys. *Nat. Commun.* **7**, 13564 (2016).
- T. Yang, S. Xia, S. Liu, C. Wang, S. Liu, Y. Fang, Y. Zhang, J. Xue, S. Yan, Y. Wang, Precipitation behavior of Al<sub>x</sub>CoCrFeNi high entropy alloys under ion irradiation. *Sci. Rep.* **6**, 32146 (2016).
- L. Koch, F. Granberg, T. Brink, D. Utt, K. Albe, F. Djurabekova, K. Nordlund, Local segregation versus irradiation effects in high-entropy alloys: Steady-state conditions in a driven system. *J. Appl. Phys.* **122**, 105106 (2017).
- O. A. Waseem, H. J. Ryu, Powder metallurgy processing of a W<sub>x</sub>TaTiVCr high-entropy alloy and its derivative alloys for fusion material applications. *Sci. Rep.* **7**, 1926 (2017).
- M. L. Jenkins, Characterisation of radiation-damage microstructures by TEM. *J. Nucl. Mater.* **216**, 124–156 (1994).
- O. El-Atwani, E. Esquivel, M. Efe, E. Aydogan, Y. Q. Wang, E. Martinez, S. A. Maloy, Loop and void damage during heavy ion irradiation on nanocrystalline and coarse grained tungsten: Microstructure, effect of dpa rate, temperature, and grain size. *Acta Mater.* **149**, 206–219 (2018).
- G. A. Vetterick, J. Gruber, P. K. Suri, J. K. Baldwin, M. A. Kirk, P. Baldo, Y. Q. Wang, A. Misra, G. J. Tucker, M. L. Taheri, Achieving radiation tolerance through non-equilibrium grain boundary structures. *Sci. Rep.* **7**, 12275 (2017).
- X. Yi, M. L. Jenkins, M. A. Kirk, Z. Zhou, S. G. Roberts, In-situ TEM studies of 150 keV W<sup>+</sup> ion irradiated W and W-alloys: Damage production and microstructural evolution. *Acta Mater.* **112**, 105–120 (2016).
- W. Setyawan, G. Nandipati, K. J. Roche, H. L. Heinisch, B. D. Wirth, R. J. Kurtz, Displacement cascades and defects annealing in tungsten, Part I: Defect database from molecular dynamics simulations. *J. Nucl. Mater.* **462**, 329–337 (2015).
- J. S. Wróbel, D. Nguyen-Manh, M. Y. Lavrentiev, M. Muzyk, S. L. Dudarev, Phase stability of ternary fcc and bcc Fe-Cr-Ni alloys. *Phys. Rev. B* **91**, 024108 (2015).
- I. Toda-Caraballo, J. S. Wróbel, S. L. Dudarev, D. Nguyen-Manh, P. E. J. Rivera-Díaz-del-Castillo, Interatomic spacing distribution in multicomponent alloys. *Acta Mater.* **97**, 156–169 (2015).
- A. Fernández-Caballero, J. S. Wróbel, P. M. Mummery, D. Nguyen-Manh, Short-range order in high entropy alloys: Theoretical formulation and application to Mo-Nb-Ta-V-W system. *J. Phase Equilibria Diffus.* **38**, 391–403 (2017).
- I. Toda-Caraballo, J. S. Wróbel, D. Nguyen-Manh, P. Pérez, P. E. J. Rivera-Díaz-del-Castillo, Simulation and modeling in high entropy alloys. *JOM* **69**, 2137–2149 (2017).
- M. Muzyk, D. Nguyen-Manh, K. J. Kurzydłowski, N. L. Baluc, S. L. Dudarev, Phase stability, point defects, and elastic properties of W-V and W-Ta alloys. *Phys. Rev. B* **84**, 104115 (2011).
- V. Blum, A. Zunger, Structural complexity in binary bcc ground states: The case of bcc Mo-Ta. *Phys. Rev. B* **69**, 020103 (2004).
- J. M. Cowley, X-ray measurement of order in single crystals of Cu<sub>3</sub>Au. *J. Appl. Phys.* **21**, 24–30 (1950).
- T. R. Waite, Theoretical treatment of the kinetics of diffusion-limited reactions. *Phys. Rev.* **107**, 463–470 (1957).
- C. S. Bescourt, C. Domain, Modeling microstructure and irradiation effects. *Metall. Mater. Trans. A* **42**, 852–870 (2011).

38. T. Suzudo, M. Yamaguchi, A. Hasegawa, Stability and mobility of rhenium and osmium in tungsten: First principles study. *Model. Simul. Mat. Sci. Eng.* **22**, 075006 (2014).
39. G.-Y. Huang, N. Juslin, B. D. Wirth, First-principles study of vacancy, interstitial, noble gas atom interstitial and vacancy clusters in bcc-W. *Comput. Mater. Sci.* **123**, 121–130 (2016).
40. J. F. Ziegler, M. D. Ziegler, J. P. Biersack, SRIM—The stopping and range of ions in matter (2010). *Nucl. Instrum. Methods Phys. Res. B* **268**, 1818–1823 (2010).
41. P. Jung, in *Atomic Defects in Metals*, H. Ullmaier, Ed. (Springer-Verlag, 1991), vol. 25, pp. 6–7; [http://materials.springer.com/lb/docs/sm:lbs\\_978-3-540-48128-7\\_6](http://materials.springer.com/lb/docs/sm:lbs_978-3-540-48128-7_6).
42. A. Devaraj, D. E. Perea, J. Liu, L. M. Gordon, T. J. Prosa, P. Parikh, D. R. Diercks, S. Meher, R. Prakash Kolli, Y. S. Meng, S. Thevuthasan, Three-dimensional nanoscale characterisation of materials by atom probe tomography. *Int. Mater. Rev.* **63**, 68–101 (2018).
43. W. C. Oliver, G. M. Pharr, Nanoindentation in materials research: Past, present, and future. *MRS Bull.* **35**, 897–907 (2010).
44. C. D. Hardie, S. G. Roberts, A. J. Bushby, Understanding the effects of ion irradiation using nanoindentation techniques. *J. Nucl. Mater.* **462**, 391–401 (2015).

**Acknowledgments:** We would like to thank P. M. Baldo and E. A. Ryan for assistance with the experiment. **Funding:** This work was supported by the U.S. Department of Energy (DOE) through the LANL. N.L. and J.K.S.B. acknowledges support from the Center for Integrated Nanotechnologies, an Office of Science User Facility operated for the U.S. Department of Energy (DOE) Office of Science. D.S. and J.S.W. acknowledge support from the Interdisciplinary Centre for Mathematical and Computational Modelling (ICM), University of Warsaw, under grant no GA69-30. LANL is operated by Triad National Security LLC for the National Nuclear Security Administration of U.S. DOE (contract no. 89233218CNA000001). Research presented in this article was supported by the Laboratory Directed Research and Development program of LANL (project no. 20160674PRD3) and the G. T. Seaborg Institute. E.M. acknowledges support from the U.S. DOE, Office of Science, Office of Fusion Energy Sciences, and Office of Advanced Scientific Computing Research through the Scientific Discovery through Advanced Computing (SciDAC) project on Plasma-Surface Interactions (award no. DE-SC0008875). This work was also supported by the U.S. DOE, Office of Nuclear Energy under DOE Idaho Operations Office (contract no. DE-AC07-05ID14517) as part of a Nuclear Science User Facilities

experiment. D.S. and J.S.W. acknowledge the financial support from the Foundation for Polish Science Grant HOMING (no. Homing/2016-1/12). The HOMING programme is cofinanced by the European Union under the European Regional Development Fund. The work at CCFE was carried out within the framework of the EUROfusion Consortium and received funding from the Euratom Research and Training Programme 2014–2018 (grant agreement no. 633053) and funding from the RCUK Energy Programme (grant no. EP/P012450/1). D.N.-M. would like to acknowledge the support from MARCONI Fusion, the high-performance computer at the CINECA headquarters in Bologna (Italy), for its provision of supercomputer resources and the Institute of Materials Science for supporting his visit to LANL. The APT sample preparation and analysis were conducted using the facilities at the Environmental Molecular Sciences Laboratory, a national scientific user facility sponsored by the DOE's Office of Biological and Environmental Research and located at Pacific Northwest National Laboratory (PNNL). APT work was funded by LDRD program at PNNL's Physical and Computational Sciences Directorate. A.D. would also like to acknowledge the PCSD seed LDRD funding for supporting this work. **Author contributions:** O.E., E.M., N.L., and S.A.M. designed the HEA and the overall scope of this work. J.K.S.B. performed the deposition process and optimized the parameters. O.E. and M.L. performed the irradiation experiments. O.E., N.L., A.D., and M.M.S. performed different parts of the characterization processes. E.M., D.S., J.S.W., and D.N.-M. performed the modeling part of this work. All authors participated in data analysis and writing of this paper. **Competing interests:** The authors declare that they have no competing interests. **Data and materials availability:** All data needed to evaluate the conclusions in the paper are present in the paper and/or the Supplementary Materials. Additional data related to this paper may be requested from the authors.

Submitted 30 August 2018

Accepted 23 January 2019

Published 1 March 2019

10.1126/sciadv.aav2002

**Citation:** O. El-Atwani, N. Li, M. Li, A. Devaraj, J. K. S. Baldwin, M. M. Schneider, D. Sobieraj, J. S. Wróbel, D. Nguyen-Manh, S. A. Maloy, E. Martinez, Outstanding radiation resistance of tungsten-based high-entropy alloys. *Sci. Adv.* **5**, eaav2002 (2019).

## Outstanding radiation resistance of tungsten-based high-entropy alloys

O. El-Atwani<sup>N</sup>, LiM. Li<sup>A</sup>, Devaraj<sup>J</sup>, K. S. Baldwin<sup>M</sup>, M. Schneider<sup>D</sup>, Sobieraj<sup>J</sup>, S. Wróbel<sup>D</sup>, Nguyen-Manh<sup>S</sup>, A. Maloy<sup>E</sup>, Martinez

*Sci. Adv.*, 5 (3), eaav2002 • DOI: 10.1126/sciadv.aav2002

**View the article online**

<https://www.science.org/doi/10.1126/sciadv.aav2002>

**Permissions**

<https://www.science.org/help/reprints-and-permissions>